

Reconnection of a kinking flux rope triggering the ejection of a microwave and hard X-ray source

I. Observations and Interpretation

M. Karlický¹, B. Kliem^{2,3,4}

Received 30 July 2009; accepted 5 July 2010

© Springer ●●●

Abstract Imaging microwave observations of an eruptive, partially occulted solar flare on 18 April 2001 suggest that the global structure of the event can be described by the helical kink instability of a twisted magnetic flux rope. This model is suggested by the inverse gamma shape of the source exhibiting crossing legs of a rising flux loop and by evidence that the legs interact at or near the crossing point. The interaction is reflected by the location of peak brightness near the crossing point and by the formation of superimposed compact nonthermal sources most likely at or near the crossing point. These sources propagate upward along both legs, merge into a single, bright source at the top of the structure, and continue to rise at a velocity $> 1000 \text{ km s}^{-1}$. The compact sources trap accelerated electrons which radiate in the radio and hard X-ray ranges. This suggests that they are plasmoids, although their internal structure is not revealed by the data. They exhibit variations of the radio brightness temperature at a characteristic time scale of $\sim 40 \text{ s}$, anti-correlated to their area, which also support their interpretation as plasmoids. Their propagation path differs from the standard scenario of plasmoid formation and propagation in the flare current sheet, suggesting the helical current sheet formed by the instability instead.

Keywords: Sun: flares – Sun: radio radiation

1. Introduction

Many solar eruptions suggest that a kinking magnetic flux rope is involved. The characteristic helical shape acquired by a rising and kinking (writhing)

¹ Astronomical Institute, Academy of Sciences of the Czech Republic, 251 65 Ondřejov, Czech Republic
(e-mail: karlicky@asu.cas.cz)

² Universität Potsdam, Institut für Physik und Astronomie, 14476 Potsdam, Germany

³ University College London, Mullard Space Science Laboratory, Holmbury St. Mary, Dorking, Surrey, RH5 6NT, UK

⁴ Naval Research Laboratory, Space Science Division, Washington, DC 20375, USA

flux loop manifests itself as a rotation of the top part of the loop leading either to a crossing of the legs (also occasionally referred to as an inverse gamma shape) or to an O shape of the loop, depending on the perspective of the observer (*e.g.*, Ji *et al.*, 2003; Romano, Contarino, and Zuccarello, 2003; Gilbert, Alexander, and Liu, 2007; Cho *et al.*, 2009). A role for the helical kink instability in initiating eruptions (Török and Kliem, 2005; Fan, 2005) is nevertheless debated, since many observations and recent modeling of filaments prior to eruption indicate subcritical values of the twist (*e.g.*, Bobra, van Ballegoijen, and DeLuca, 2008). It is possible, however, that much of the twist in erupting flux ropes is built up in the early phases of the eruption through the addition of current-carrying flux by reconnection under the rope (*e.g.*, Lin, Raymond, and van Ballegoijen, 2004). Moreover, filaments outline only a small fraction of the current-carrying flux in an active region, so that part of the existing twist may remain undetected. An example is the filament in NOAA active region (AR) 10930, which did not appear particularly twisted (Williams *et al.*, 2009), although the sunspot near one end of the filament did rotate by 540° before the region erupted (Min and Chae, 2009). A second reason for questioning the occurrence of the instability lies in the fact that the writhing and apex rotation of the flux loop may also be caused by the shear field component of the ambient field (pointing along the polarity inversion line of the photospheric flux) if a process other than this instability accelerates the loop upwards (Isenberg and Forbes, 2007). The upward acceleration may be caused by the torus instability (Kliem and Török, 2006; Török and Kliem, 2007). On the other hand, many erupting filaments exhibit clear indications for *both*, an overall helical shape, *i.e.*, a writhed axis, and a winding of the threads in the filament about the axis, *i.e.*, twist; this combination supports the occurrence of the helical kink mode strongly. A particularly clear case was described by Romano, Contarino, and Zuccarello (2003), who estimated a twist of $\sim 10\pi$ in a filament early in its eruption. The twist decreased subsequently, as expected for a helical kink. Indications for high twist values in prominences near the onset of an eruption, including estimates made before the onset and in agreement with stability estimates for the helical kink mode, were presented by Vršnak, Ruždjak, and Rompolt (1991) and Vršnak *et al.* (1993).

Usually, the leg crossing is a pure projection effect, expected for any writhing loop independent of the cause of the writhing, provided the observer has an appropriate perspective on the eruption. For moderately supercritical values of the twist, $\Phi \sim (3-5)\pi$, such that the loop develops about one helical turn in total (*i.e.*, the perturbation has a normalized axial wavenumber $k' = kl/2\pi \sim 1$, where l is the length of the flux loop), the helical kink actually drives the legs *away* from each other. The front leg is then moving toward the observer and the rear leg is moving away (see, *e.g.*, Fig. 4 in Török and Kliem, 2005 and Fig. 14 in Green *et al.*, 2007). A completely similar motion of the legs results from the writhing that is caused by the shear field. However, the eruptive flare on 18 April 2001 in AR 9415, whose microwave emissions are studied in the present paper, did not only develop an inverse gamma shape but also gave indications that the crossing legs indeed interacted, producing superimposed sources and nonthermal particles. The superimposed, relatively compact microwave and hard X-ray sources originated near the crossing point and propagated along the legs to

the top of the erupting loop. We point out, and demonstrate through numerical simulation in the companion paper (Kliem *et al.*, 2010; hereafter Paper II), that the interaction of crossing legs can result from the helical kink instability of a flux rope if modes with $k' \sim 2$ are dominant as a result of high initial twist in the range $\Phi \gtrsim 6\pi$.

The superimposed, propagating sources of the microwave and hard X-ray emission represent a second interesting aspect of the event under investigation. These “blobs” trap the accelerated particles, which is a known property of plasmoids (*e.g.*, Karlický and Bárta, 2007). X-ray sources of the same or similar nature have been known for a long time. They have first been recognized in association with so-called long-duration events (*e.g.*, Hudson, 1994; Švestka *et al.*, 1995). Similar X-ray plasma ejections have later been found also in impulsive, compact flares (*e.g.*, Shibata *et al.*, 1995; Nitta, 1996; Tsuneta, 1997; Ohya and Shibata, 1997; Ohya *et al.*, 1997). Based on this fact, Ohya and Shibata (1998) and Shibata and Tanuma (2001) proposed a general scenario of plasmoid formation and ejection. They assumed that an extended (flare) current sheet is formed below a rising magnetic flux rope. Magnetic islands (plasmoids) are formed in this current sheet, due to the tearing-mode instability, and move along the sheet, possibly coalescing into larger units. Furthermore, a close temporal association between plasmoid ejections and so-called drifting pulsation structures was found. These are observed in dynamic radio spectra in the ~ 600 – 2000 MHz range. Their origin was related to quasi-periodic episodes of particle acceleration in an intermittent (“bursty”) mode of reconnection in the flare current sheet, combined with the trapping of the accelerated particles in the resulting plasmoids (Kliem, Karlický, and Benz, 2000; Karlický, 2004; Karlický, Fárník, and Krucker, 2004; Karlický and Bárta, 2007). In all these cases, the formation and motion of plasmoids is supposed to occur in the vertical flare current sheet *below* a rising flux rope (which often contains a filament or prominence). The superimposed sources in the 18 April 2001 flare, however, did clearly propagate along the legs to the top of the rising loop.

In this paper we present a detailed analysis of the microwave observations in the course of the eruptive flare. The imaging data were taken by the Nobeyama Radioheliograph at 17 and 34 GHz. They are complemented by light curves from the Nobeyama Radiopolarimeters and by a dynamic spectrum of the dm–Dm emission obtained by the HiRAS spectrograph. This event was already studied by Hudson *et al.* (2001), who investigated the fast coronal ejection in hard X-rays, observed in the 23–53 keV energy range by the *Yohkoh* Hard X-ray Telescope, joint with the strongest moving source mapped by the Nobeyama Radioheliograph. However, they did not analyze the evolution that led to the formation of the ejected source, which is suggestive of a plasmoid or similar structure in, or in the vicinity, of an erupting, kinking flux rope, different from the classical picture of formation in the flare current sheet.

Paper II presents MHD simulations of the helical kink instability of a highly twisted flux rope, which corroborate the model of reconnection between flux rope legs suggested by the present data analysis.

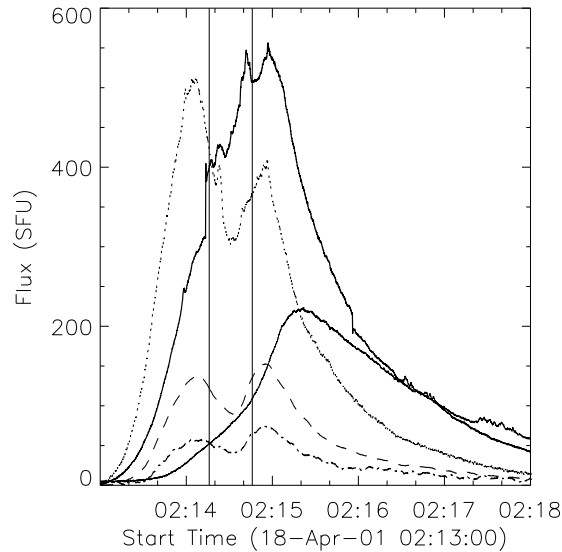


Figure 1. Centimeter–decimeter time profiles of the 18 April 2001 flare observed by the Nobeyama Radiopolarimeters at the frequencies 1 GHz (thin solid line), 2 GHz (thick solid), 3.75 GHz (dotted), 9.4 GHz (dashed), and 17 GHz (dot-dashed). Background fluxes are subtracted. The two vertical lines mark the times of the first and second (main) 23–33 keV hard X-ray flux maxima given in Hudson *et al.* (2001).

2. Observations and Interpretation

The 18 April 2001 flare, classified as *GOES* C2.2, occurred in NOAA AR 9415 at a location $\approx 26^\circ$ behind the west limb, corresponding to a radial occultation height of ≈ 110 arcsec (Hudson *et al.*, 2001). Its temporal evolution observed by the Nobeyama Radiopolarimeters at 1, 2, 3.75, 9.4, and 17 GHz is shown in Figure 1. The higher frequencies reveal two peaks, around 02:14:10 and 02:14:55 UT, whereas only the second, main peak is seen at the lower frequencies (which show a steeper rise at the time of the first peak). This structure is due to the rise of different parts of the microwave source above the limb as well as to intrinsic variations in the source, and it is similar to the light curves in the hard and soft X-ray ranges, respectively (see Fig. 1 in Hudson *et al.*, 2001). The main peak shows a systematic delay toward lower frequencies, which can be related to a change from free-free emission at microwaves to plasma emission at decimetric wavelengths (see the description of the dynamic radio spectrum below).

We searched for any phenomena at earlier times, which might yield clues to the onset of this behind-limb event. The *SOHO*/EIT images at 01:25:58, 01:35:19, 01:48:12, 02:00:11, and 02:12:10 UT show no structural changes above the solar limb at position angles near the eruption. Only a weak jet was found about 100 arcsecs northwards from this location in the 01:48:12 UT image, too early to provide an immediate trigger of the fast eruption.

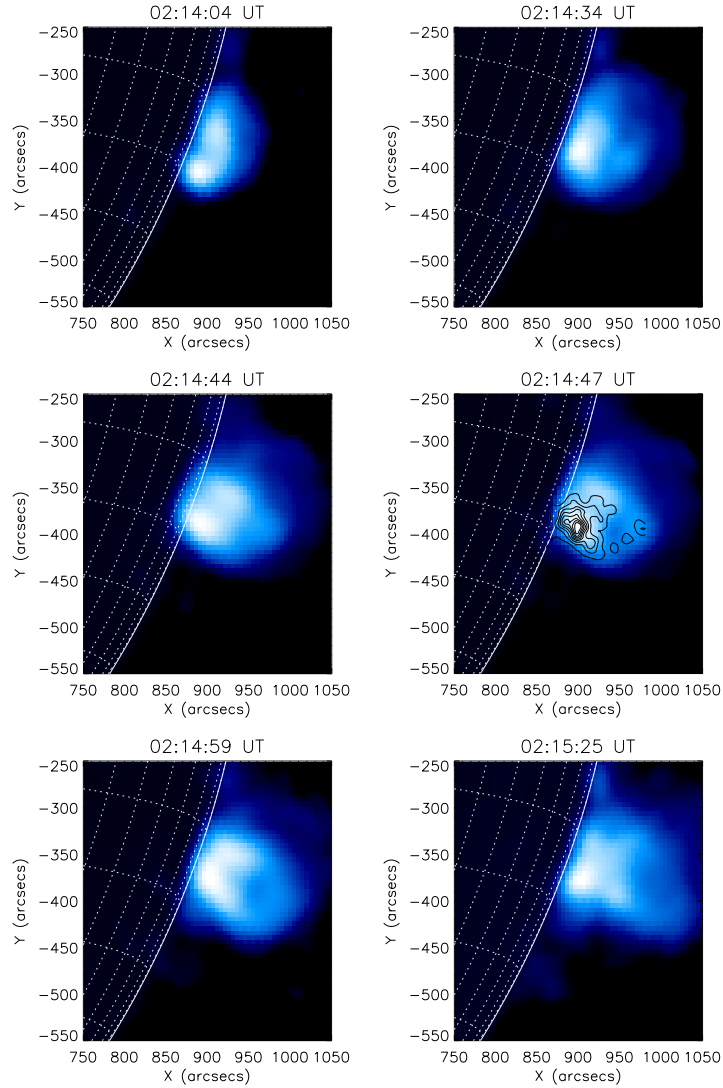


Figure 2. 17 GHz Nobeyama Radioheliograph images of the 18 April 2001 flare comprising the period of the two peaks in the microwave and hard X-ray time profiles. Logarithmic brightness temperature in the range $8000\text{--}10^6$ K is displayed, and 23–33 keV contours of the hard X-ray source at the time of peak brightness are overlaid on the simultaneous 17 GHz image. The sequence shows the rise of the main, inverse gamma shaped microwave source above the solar limb and the proximity of the brightest microwave and hard X-ray emission to the crossing point.

Similarly, the EIT images taken during and after the event at 12 min cadence in the 195 \AA band do not reveal any flare-related features, most likely because of the behind-limb location.

The evolution of the flare observed by the Nobeyama Radioheliograph at 17 GHz with a spatial resolution of 10 arcsec in the interval 02:14:04–02:15:25 UT

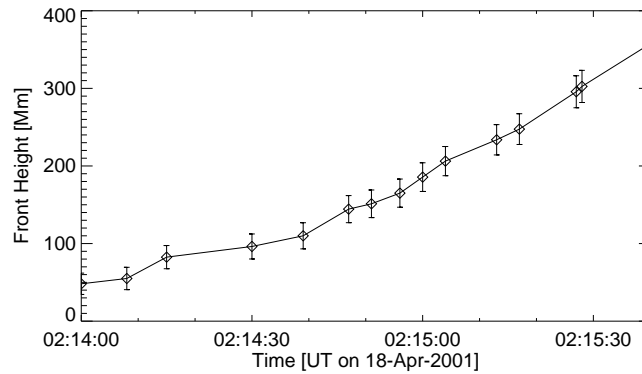


Figure 3. Rise profile of the front edge of the inverse gamma shaped main microwave source at 17 GHz.

is presented in Figure 2. Overall, the microwave source exhibits a rapid evolution, indicative of a rather unstable configuration. By about 02:14:04 UT, the time of the first microwave and hard X-ray peak, the source has developed into the top part of a single flare loop. Then it changes to concave shape, accompanied by weak, diffuse emission at greater heights (02:14:34 UT). With the second rise of the flux, the diffuse emission turns into a clearer loop shape, now in the form of a complete ellipse (02:14:59 UT). Next a cross appears above the limb as the ellipse rises further (02:15:25 UT). This configuration is similar to the inverse gamma shape observed in strongly kinking filaments. The peak microwave emission is located very near the crossing point, and the rise of the crossing point above the limb is associated with the main peak of the 17 GHz light curve (Figure 1). After $\sim 02:16$ UT the upper part of the inverse gamma shaped main microwave source faded to fall out of the dynamic range of the radio images, but the source remained bright at the limb near the original position of the crossing point, as if the crossing point did not participate in the subsequent expansion. Rather, the location of peak brightness at the limb is consistent with a slight retraction of the crossing point to or even behind the limb (Figures 4 and 5).

For comparison, the contours of the 23–33 keV source at the time of the main hard X-ray flux peak (02:14:47 UT) are overlaid on the simultaneous microwave image in Figure 2. The overlay shows that the hard X-ray source emerges from about the position of the crossing legs of the rising loop. At this time it is not tied to the loop top. This renders an association with a shock, which might be driven by the rising loop, to be unlikely. Also, the motion of the X-ray source changes from a slow rise, still staying near the limb (consistent with occultation of the source’s main part), to a fast one at about this time. The fast rise can be fit by a linear function to yield a velocity of $\approx 930 \text{ km s}^{-1}$; see Fig. 3 in Hudson *et al.* (2001). In other words, the main acceleration of this source ended shortly after the main hard X-ray peak, as is typical of fast ejections (*e.g.*, Zhang and Dere, 2006; Temmer *et al.*, 2008). Hudson *et al.* (2001) also show that the relatively compact hard X-ray source is nonthermal, with a power-law spectrum in the range $\sim 23\text{--}93$ keV, throughout the period it could be detected ($\approx 02:13:50\text{--}02:17$ UT).

In order to estimate the main acceleration of the inverse gamma shaped microwave source, images sharper than those in Figure 2 are required. These are obtained by employing a different weighting of the visibilities provided by the interferometer (see Figure 5 below). The front height of the source vs. time and the corresponding errors can then roughly be estimated in the period 02:14–02:15:40 UT (Figure 3). Although the data scatter substantially, it is obvious that the acceleration extended up to \sim 02:15:20 UT and peaked at about 02:14:45 UT, very close to the time of peak hard X-ray flux; even a secondary jump in velocity at the time of the first hard X-ray maximum can be seen.

Isolated rising blobs of microwave emission, superimposed on the fading inverse gamma shaped main source, became discernible soon after the crossing point had appeared above the limb. We term these sources “compact”, although they are not necessarily below the resolution limit of the interferometer at all times. Two of them occurred slightly above the cross, one in each of the crossed legs, at about 02:15:33 UT (marked by arrows in Figures 4 and 5), which is shortly after the main acceleration of the ejecta. The brighter one, in the southern leg of the erupting loop, was co-spatial with the nonthermal hard X-ray source (see Figs. 1–3 in Hudson *et al.*, 2001). The images between 02:15:49 and 02:16:15 UT in Figures 4 and 5 show that even a series of compact sources formed, their location being consistent with an arrangement along the rising loop above the crossing point. The sources moved upward and merged near the top of the loop, where a single source remained after 02:16:35 UT (see the images after 02:16:15 UT in Figures 4 and 5). The final compact source continued its rise at high speed, evolving into a fast coronal mass ejection (CME).

Figure 6 displays the east-west position of the final compact source vs. time, along with its maximum brightness temperature and its area at half the peak brightness temperature. It is seen that the source continued its westward rise at the high projected speed of $\gtrsim 1000 \text{ km s}^{-1}$ obtained from the hard X-ray images up to 02:15:45 UT in Hudson *et al.* (2001). The westward rise is close to the initial direction of the CME and at about half the projected velocity of the CME leading edge (estimated to be $\approx 2500 \text{ km s}^{-1}$ in the LASCO CME catalogue at NASA’s CDAW data center, <http://cdaw.gsfc.nasa.gov>). This lies within the range of core and leading-edge velocity ratios observed in fast CMEs (Maričić, Vršnak, and Roša, 2009). As expected from the high rise velocity, the formation of a large-scale coronal shock is indicated by an associated slow-drift (type II) burst commencing at \approx 02:20 UT near 300 MHz; see the dynamic spectrum in Figure 7.

In addition to the bright type II burst, a weaker continuum can be discerned in the dynamic spectrum from about 02:14 UT onward. The continuum had a starting frequency near 2 GHz and drifted to lower frequencies at an intermediate rate, such that its trace arrived near but above the frequency of the type II burst (by a factor 1.5–2) when that burst commenced. Its sharp onset in the 2 GHz time profile, as well as the delayed onset in the 1 GHz profile, are also clearly visible in Figure 1. It is plausible to assume that the drifting continuum is caused by plasma emission (near the electron plasma frequency or its harmonic) associated with the appearance of the leg crossing above the limb and with the compact

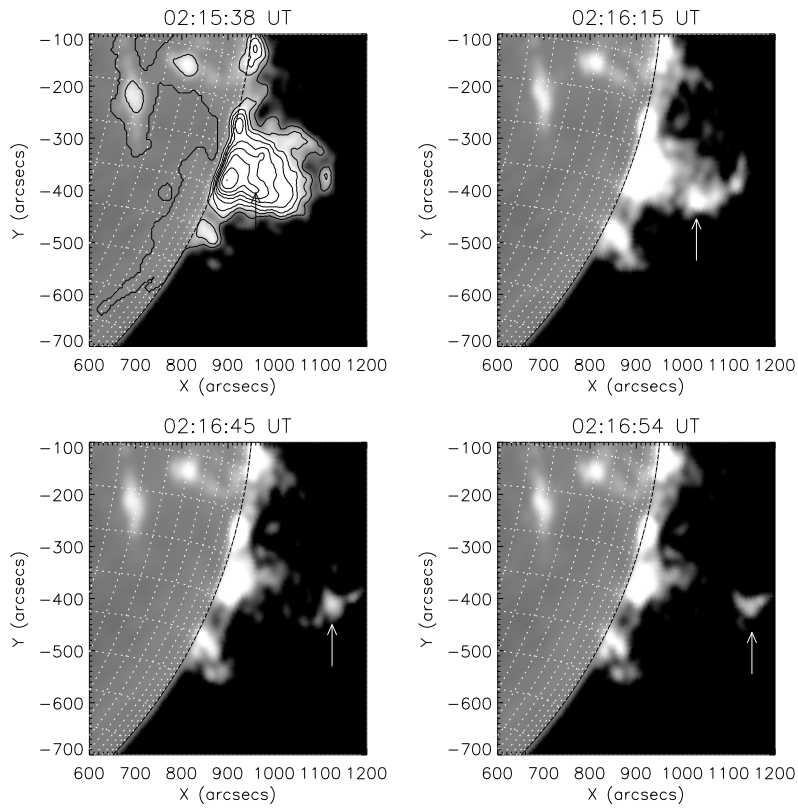


Figure 4. 17 GHz Nobeyama Radioheliograph images comprising the period of the rapidly rising, superimposed compact sources. Logarithmic brightness temperature in the range 6000–20,000 K is displayed in grayscale, with contours of logarithmic brightness in the range 8000– 10^6 K overplotted on the first image. White arrows in panels 2–4 mark the brightest compact source. The black arrow in panel 1 marks the position of the brightest 23–33 keV hard X-ray source at the same time, which coincides with the brightest compact microwave source (see Figs. 2 and 3 in Hudson *et al.*, 2001).

microwave/hard X-ray sources. This interpretation implies high densities, starting slightly above 10^{10} cm^{-3} (adopting the harmonic assumption) and gradually decreasing to $n_e \sim 7$, 4, and $1 \times 10^9 \text{ cm}^{-3}$ by 02:15:30, 02:16, and 02:17 UT, respectively. These values are consistent with the independent estimate of the source density of $\lesssim 4 \times 10^9 \text{ cm}^{-3}$ at $\approx 02:15:45$ UT in Hudson *et al.* (2001), who used the expression for the brightness temperature of free-free emission joint with estimates of source temperature and depth of the brightest compact 17 GHz source (see below for the expression). High densities support the assumption that the compact sources are plasmoids.

The 17 GHz emission of the brightest compact source is unpolarized and the spectral index α between 17 and 34 GHz increases from zero at 02:16 UT to $\alpha = 2.1$ at 02:17 UT. This shows that the optically thin free-free emission at 02:16 UT changes into optically thick free-free emission at 02:17 UT. In the

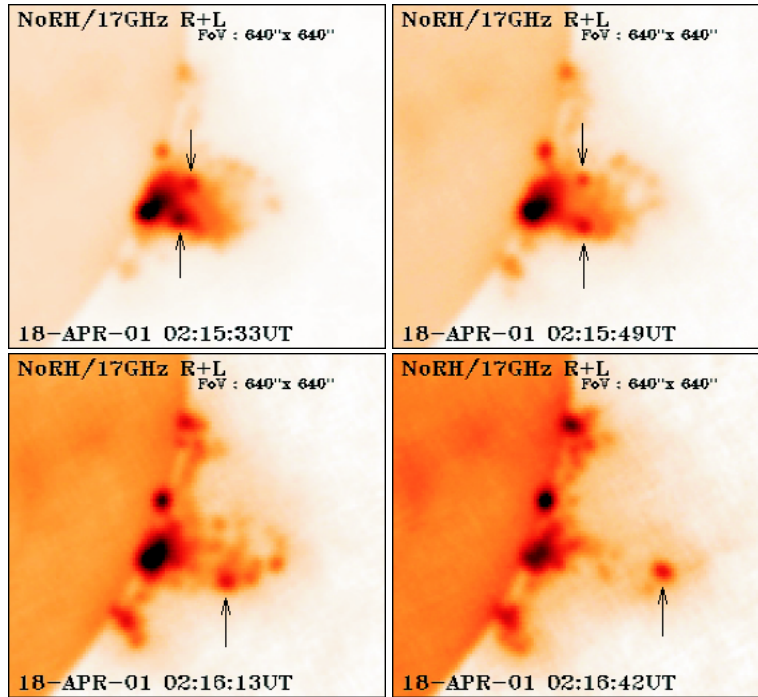


Figure 5. Similar to Figure 4, with different weighting of the visibilities to emphasize small scale structure (courtesy of M. Shimojo). A series of upward moving compact sources, arranged along the upper loop of the main, inverse gamma shaped source, is now apparent, the brightest of which are marked by arrows. All compact sources merge eventually at the top of the main microwave source (final panel), continuing the rapid ascent.

optically thin case, we can estimate the kinetic temperature of the electrons in the thermal background plasma from the relation $T_e = (0.2dn_e^2/(f^2T_b))^2$, where d is the source depth, roughly estimated from the source area A as $d \sim A^{1/2}$, f is the observing frequency, and T_b is the observed brightness temperature (see the relations (7), (13), and (21) in Dulk, 1985). The kinetic temperature in the source at 02:16 UT thus obtained is $T_e \approx 2 \times 10^5$ K.

The brightness temperature and area of the final compact source plotted in Figure 6 are seen to vary, essentially in anti-phase, with a characteristic time scale of ~ 40 s. The amplitudes of the variation are $T_{b\max}/T_{b\min} \approx 1.3$ and $A_{\max}/A_{\min} \approx 2$. We check whether these values are consistent with the assumption of perpendicular adiabatic compression and rarefaction. Such behavior was observed in MHD simulations of plasmoids produced by tearing and coalescence of magnetic islands in a current sheet (see, *e.g.*, Fig. 5 in Schumacher and Kliem, 1997). The characteristic time scale for the oscillations of coalesced islands was found to be a few (~ 3 – 5) Alfvén transit times across the island in the direction of the current sheet. From Figure 6 we have a source diameter of ~ 25 Mm. Using $V_A = 1000 \text{ km s}^{-1}$ as a typical value for the Alfvén velocity in the lower corona, an Alfvén transit time of 25 s is obtained, a factor 2–3 larger than the value

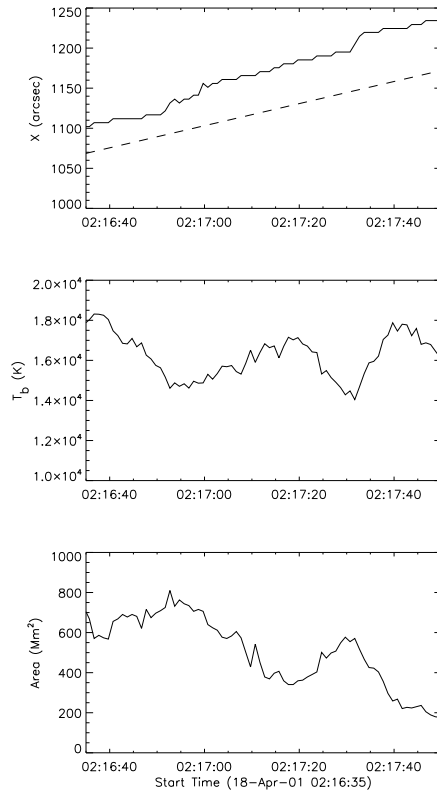


Figure 6. Evolution of the final compact 17 GHz source in the interval 02:16:35–02:17:50 UT, *i.e.*, after the merging of all rising blobs into a single source. *Top*: Solid line: east-west source location. For comparison, the dashed line represents a velocity of 1000 km s^{-1} . *Middle*: Maximum brightness temperature. *Bottom*: Source area at half the peak brightness temperature.

suggested by the above simulation. Given that further assumptions and idealizations enter the comparison (*e.g.*, the 2D idealization of the simulation), we consider this level of mismatch to be still consistent with the assumption of perpendicular adiabatic compression and rarefaction. This process leaves $d \approx \text{const}$ with $n \propto A^{-1} \propto B$, where B is the field strength in the plasmoid. The first adiabatic invariant states for the perpendicular temperature $T_{\perp}/B = \text{const}$. For a perpendicular adiabatic compression which reduces A by a factor 2, as estimated from Figure 6, the density and field strength are doubled, while the temperature $T = (2T_{\perp} + T_{\parallel})/3$ rises by a factor $5/3$, not too different from the observed increase by a factor 1.3. Here we have assumed $T_e \approx T_b$, *i.e.*, optically thick emission, which is appropriate for the time range of Figure 6, as discussed above. In summary, both the period and the amplitude variations, although not giving a clear agreement, are consistent with the assumption of perpendicular adiabatic compression of a plasmoid within the substantial uncertainties of the estimates.

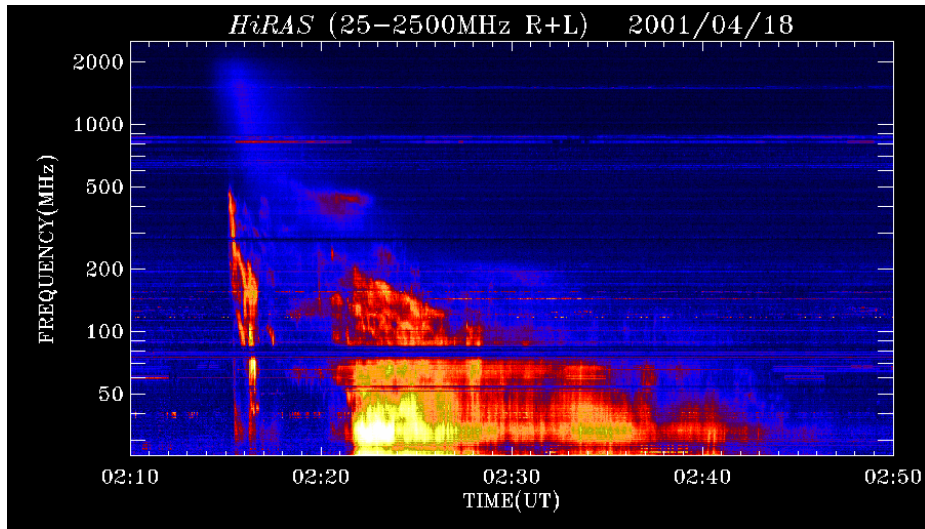


Figure 7. Dynamic spectrum from the HiRAS Spectrometer, showing the bright slow-drift (type II) burst indicative of a CME-driven coronal shock wave (starting at \approx [02:20 UT, 300 MHz]), the weaker drifting continuum likely associated with the ejected microwave and hard X-ray sources (starting at \approx [02:14 UT, 2000 MHz]), and the group of fast-drift (type III) bursts (starting at \approx [02:15 UT, 500 MHz]).

The dynamic radio spectrum in Figure 7 further shows a group of fast-drift (type III) bursts starting in the 500–200 MHz range in the interval 02:15–02:17 UT, which also reveal the acceleration of nonthermal electrons at about the time the cross in the microwave source appeared at the limb and through the subsequent phase characterized by moving compact microwave and hard X-ray sources. Additionally, they indicate that a minor part of the nonthermal electrons could escape along open field lines.

Figure 8 summarizes the evolutionary sequence of the main and compact microwave sources as suggested by the observations. The evolving shape of the source is compared in Figure 9 with a kink-unstable erupting flux rope, seen from a similar perspective. The overall qualitative agreement, due to the expansion and strong writhing of the flux rope in the course of its rise, is apparent.

This simulation, introduced in detail in Paper II, also supports the interpretations that the formation of compact sources, which propagated along the legs to the top of the erupting structure, resulted from the interaction of the legs of a kinking flux rope near the observed crossing point, and that these sources were plasmoids. Figure 10 shows that the kinking and rising flux rope triggers the formation of a helical current sheet in addition to the formation of the vertical (flare) current sheet. The helical current sheet wraps around the legs and passes over the upper section of the flux rope in the interface to the ambient field. As the flux rope legs approach each other, the vertical current sheet shrinks and the two layers of the helical current sheet come into contact in its place. In the height range where this happens, they reconnect with each other, transiently forming a single-layer current sheet, which is subsequently squeezed

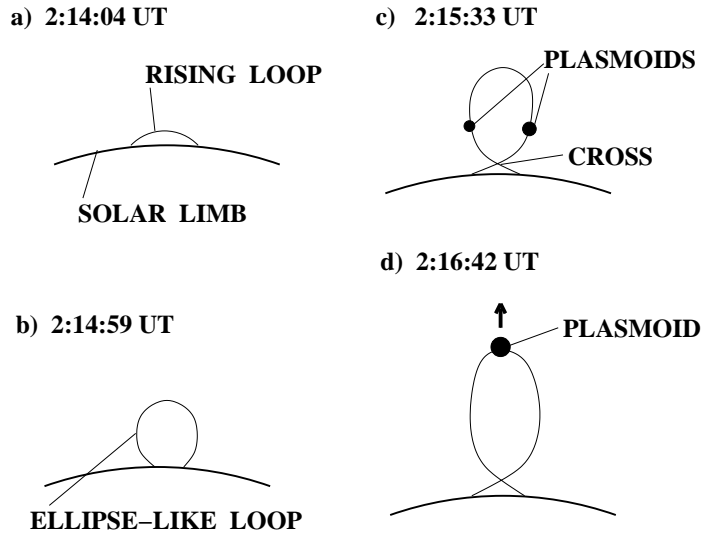


Figure 8. Schematic summary of the flare evolution at 17 GHz. The compact rising sources, the brightest of which is co-spatial to the hard X-ray source, are suggested to be plasmoids.

and destroyed between the partially merging flux rope legs (Figure 11). Thus, “standard flare reconnection” in the vertical current sheet is superseded in the simulation by reconnection involving the helical current sheet and the flux rope legs.

The two layers of the helical current sheet begin to come into contact and to reconnect at $t \approx 20$ Alfvén times. This leads to the complete removal of the vertical current sheet by $t \approx 24$. Subsequently, the flux originally in the legs of the rope reconnects, partly between the legs, partly with the ambient field (see Fig. 3 in Paper II for an illustration). The transition of the reconnection from the vertical to the helical current sheet thus occurs between the second and third snapshot pair in Figure 9, corresponding to $\sim 02:14:30$ – $02:15:00$ UT. The helical current sheet becomes the site of dominant reconnection in the system in this period and remains so for a period of $\lesssim 10$ Alfvén times until the current channel in the core of the flux rope, which is seen in Figures 10 and 11, begins to reconnect in the full height range of its approach. Thus, in both data and simulation, the reconnection in the helical current sheet is dominant just after the upward acceleration of the ejection has reached its peak, including the beginning propagation phase after the main acceleration (see the rise profile of the flux rope in Paper II). The corresponding period in the observations extends from the time the hard X-ray source began its rapid ascend ($\approx 02:14:45$ UT) till and somewhat beyond the formation of the strongest compact microwave sources ($\approx 02:15:30$ UT). From this timing and from the path of the hard X-ray and compact microwave sources—from the crossing point, along the legs, and to the apex of the flux rope—we conjecture that reconnection in the helical current sheet formed plasmoids which subsequently propagated along the helical current sheet and became visible as these radiation sources by trapping nonthermal particles.

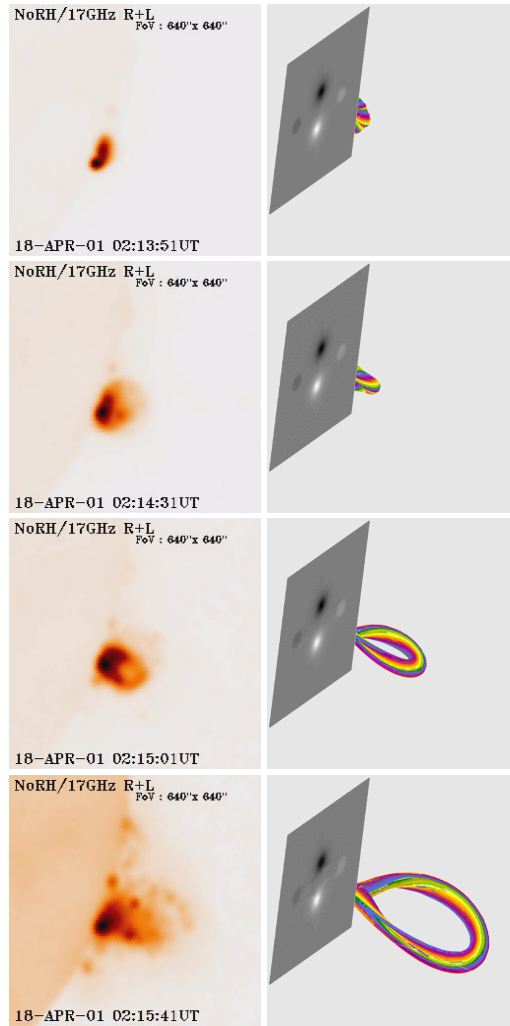


Figure 9. Comparison of the evolving 17 GHz source with the shape of a simulated kink-unstable flux rope displayed at the same viewing angle (tilted away from the observer by 26° , so that the magnetogram, $B_z(x, y, 0, t)$, is seen from the bottom side). The flux rope has an initial twist of 6π and is also torus unstable. Snapshots of field lines in the core of the flux rope, started at circles at the apex, are shown at the times $t = 9.1, 18.0, 23.6,$ and $28.6\tau_A$ (Alfvén times), corresponding to apex heights $h_a = 1.1, 1.4, 2.8,$ and $4.5h_0$, respectively. See Paper II for the details of the simulation, including the rise profile $h_a(t)$ and the choice of the initial equilibrium.

This does not exclude that the major part of the emitting nonthermal particles was actually accelerated by reconnection in the vertical current sheet, as suggested by the standard flare picture. The major part of the hard X-rays and microwaves is emitted simultaneously with the main CME acceleration (compare Figure 1 and Fig. 1 in Hudson *et al.*, 2001 with Figure 3). The main acceleration of fast CMEs is often synchronized with flare reconnection, though

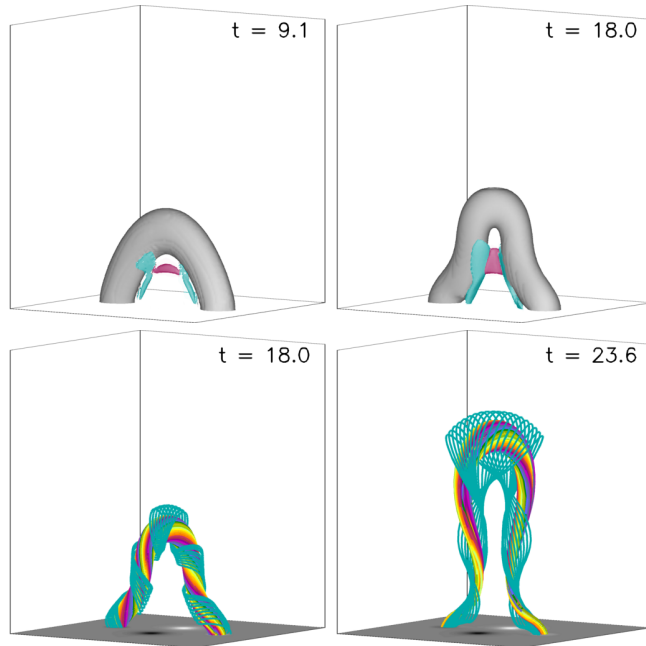


Figure 10. Formation of the helical and vertical current sheets, and beginning destruction of the vertical current sheet by the approaching legs of the kinking flux rope shown in Figure 9. Isosurfaces of current density $|\mathbf{J}(\mathbf{x}, t)|$ are displayed in the top panels; they show the current channel in the core of the flux rope (gray), the helical current sheet (cyan), and the vertical current sheet (red). The isosurfaces show only the bottom part of the helical current sheet, where the current density is highest. Field lines of the current density $\mathbf{J}(\mathbf{x}, t)$ are therefore plotted in the bottom panels to show the path of the whole helical current sheet (cyan). The core of the flux rope is displayed in these plots in the same manner as in Figure 9. The final panel displays field lines in the inflow region of the reconnection in the helical current sheet (between the current sheet and the surface of the current channel) because part of the field lines *in* the current sheet already connect to the ambient field at this time, as a result of the reconnection. A cubic inner subvolume of the simulation box is displayed, and the magnetogram, $B_z(x, y, 0, t)$, is included in the field line plots.

to occur in the vertical current sheet (*e.g.*, Lin and Forbes, 2000; Qiu *et al.*, 2004; Zhang and Dere, 2006), and this is the case also in the simulation shown in Figures 9–11. Most of the flux rope’s acceleration is complete before the helical current sheet begins to reconnect strongly. However, the comparison of the data with the simulation suggests that it is the replacement of the vertical current sheet by the helical current sheet which allows a large part of these particles to become trapped and propagate to the top of the erupting flux rope. The acceleration of particles continues past the suggested transition of reconnection from the vertical to the helical current sheet, as evidenced by continuing strong microwave emission from the limb source (near the crossing point) and by the creation of fast-drift bursts through 02:17 UT.

Finally, the reconnection between the legs of the kinking flux rope commences and remains at low heights (see Figures 9–10 and the detailed consideration in Paper II). This is consistent with the location of peak emission in the main microwave source near the limb throughout the event.

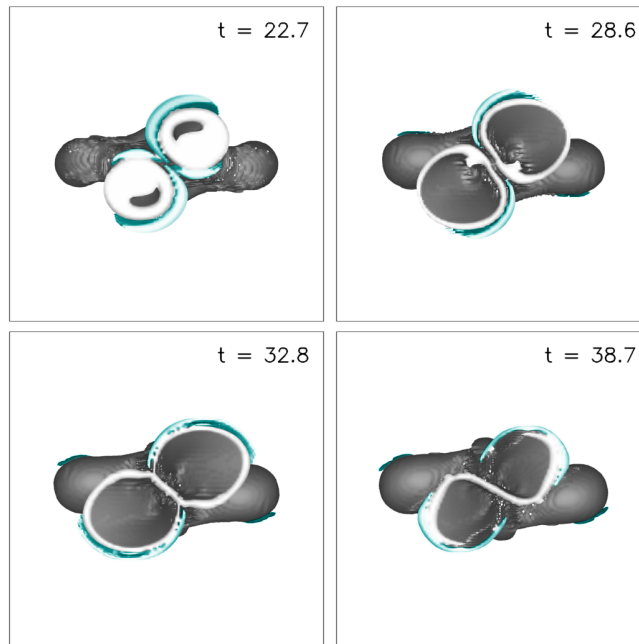


Figure 11. Approach and reconnection of the helical current sheet (cyan) and of the legs of the kinking flux rope (gray) shown in Figures 9–10, visualized by isosurfaces of current density. Vertical views at the volume below a horizontal cut plane at the height of 1.5 times the initial flux rope apex height h_0 are shown. The current channel of the employed Titov-Démoulin flux rope has the property that the highest current density is located at its surface. This property amplifies in the course of the dynamical evolution, leading to an apparently hollow structure of the current channel. However, current is flowing in the entire cross section of the channel. See Fig. 4 in Paper II for perspective views of a similar simulation run.

3. Discussion

The inverse gamma shape of the main microwave source, revealed by the 17 GHz images in Figure 2, suggests that the erupting flux was loop shaped and experienced a strong writhing in the course of its rise. This writhing is consistent with both possible causes, the occurrence of the helical kink instability, and the lateral forces acting on the legs of the loop due to a shear field component of the ambient field if the loop is accelerated by another process.

However, the strongest microwave and hard X-ray sources provide evidence that the legs of the rising flux loop did interact near the point of their crossing (as seen in the projection onto the plane of the sky). Magnetic reconnection is the prime candidate for such interaction, which is confirmed by the numerical simulations in Figures 9–11 and Paper II. These simulations demonstrate that the legs of a writhing flux loop approach each other and reconnect only if the deformation is a double helix (normalized axial wavenumber $k' \sim 2$). This cannot be achieved through the writhing by a shear field component and implies the occurrence of the helical kink instability of a flux rope that has an initial twist of $\approx 6\pi$ or higher.

The observation data do not allow to determine whether such a twist could accumulate prior to the eruption, or was built up in the early phase of the eruption.

Three pieces of evidence suggest strongly that nonthermal particles were accelerated, and compact propagating sources were formed, at or near the crossing point. First, the point of peak brightness of the microwave source stayed close to the crossing point throughout the event. Second, part of the nonthermal particle population became trapped in compact microwave and hard X-ray sources whose first appearance and motion suggest an origin associated with the legs of the erupting flux loop, near the crossing point, and near or shortly after the time of peak energy release rate (peak hard X-ray flux). A coincidental association with the rise of the crossing point above the limb and the hard X-ray peak, implying an origin of the compact sources at earlier times from below the crossing point, cannot be excluded, due to the occultation of the lower parts of the flaring volume. However, we regard such a coincidence to be far less likely. The simultaneous occurrence of the first two compact microwave sources in the two legs slightly above the crossing point, with similar distances and velocities, argues against a coincidence in particular. Third, the escaping part of the nonthermal particles was first detected through its fast-drift emission (type III bursts) at meter wavelengths at the time the crossing point had appeared at the limb.

The subsequent rapid fading of the upper part of the inverse gamma shaped main microwave source is consistent with the scenario that the interaction of the flux rope legs caused a breakup of the original rope, as suggested for another event by Cho *et al.* (2009) and as also indicated by the numerical simulations in Paper II. However, the fading can also be explained simply as a consequence of the upward expansion of the source, which causes the field strength and density in the flux loop to decrease. The occultation of the source's lower part prevents a decision between these possibilities.

The interpretation of the moving compact microwave and hard X-ray sources as plasmoids is not proven by the available data, but it is supported by several aspects. First, the localization in the course of propagation across the substantial height range of several 100 Mm requires a high efficiency of particle trapping, which is a known property of plasmoids. Alternative structures—solitons or shocks—are likely less efficient in trapping the nonthermal particles. Second, the observed parameters of the source oscillations are roughly consistent with the assumption of perpendicular adiabatic compression and rarefaction. This is a typical behavior of plasmoids created by island coalescence in a current sheet. Third, the region of plasmoid formation and their trajectories correspond to a current sheet computed in the model: the helical current sheet. It has been demonstrated in a long series of investigations that plasmoids are formed and propagate in reconnecting current sheets, due to the tearing and coalescence instabilities (see, *e.g.*, Leboeuf, Tajima and Dawson, 1982; Matthaeus and Lamkin, 1986; Scholer and Roth, 1987; Schumacher and Kliem, 1996; Magara, Shibata, and Yokoyama, 1997; Shibata and Tanuma, 2001; Loureiro, Schekochihin and Cowley, 2007; Karlický and Bárta, 2007; Bárta, Vrsňak, and Karlický, 2008; Bhattacharjee *et al.*, 2009; Bárta, Büchner and Karlický, 2010; Edmondson *et al.*, 2010). All these investigations were performed for the geometry of a plane (single or double) current

sheet, but they span a very wide range of parameters and applications and use a variety of different methods; the most recent one is even three-dimensional. Therefore, the formation and acceleration of plasmoids is established as an important process in the dynamics of reconnecting current sheets. The simulations presented in Figures 9–11 and Paper II are fully three-dimensional and model the instability of a flux rope at active-region scales, so that they necessarily lack the resolution required to demonstrate the conjectured process of plasmoid formation in the thin helical current sheet. However, the general evidence provided by the quoted investigations (and references therein) supports our conjecture (see also Paper II).

Furthermore, as shown by Bárta, Vrsňak, and Karlický (2008), plasmoids formed in the reconnection region of an eruptive flare move upward if the magnetic field surrounding them diverges in the upward direction. This is the natural situation in the solar atmosphere and explains why most plasmoids move upward. For the same reason, a plasmoid that has moved to the top of an erupting flux rope (in the helical current sheet in the present case) will remain there and continue its upward motion joint with the rope.

Can plasmoid formation in the vertical current sheet according to the standard scenario (Ohyama and Shibata, 1998) also be consistent with the observations of the event? In this case it remains unclear how the plasmoids could find a path to the top of the rope which first follows the legs. The field lines reconnected in the vertical current sheet pass near the apex of the rope only if the shear field component of the ambient field is weak, but in this case the plasmoids propagate essentially vertically between the legs without approaching them. If the shear field component is significant, then the field lines reconnected in the vertical current sheet do wrap around the legs of the flux rope (opening a path for plasmoids and accelerated particles to the legs), but from there they continue downward to the photosphere, *not* to the apex of the flux rope (see, *e.g.*, Figs. 3 and 4 in Kliem, Titov, and Török, 2004 for a field line plot of such a configuration).

Finally, we consider an alternative mechanism for the formation of localized, traveling structures in the legs of an erupting flux rope. If the reconnection in the vertical current sheet under the rising flux rope does not only merge pairs of field lines that are both external to the rope, but also field lines in the legs of the rope with field lines of the ambient field, then relatively sharp bends can temporarily occur in the reconnected field lines in the legs. The bends move upward along the legs as the newly reconnected field lines relax to a less bent shape. Special requirements on the driving mechanism of the eruption, for example a high initial twist, are not implied. Figure 12 gives an illustration taken from a run that does not involve the helical kink instability (from Schrijver *et al.*, 2008a); note that the bends appear sharper than in reality due to the projection. While this mechanism is consistent with the formation site and path of the compact microwave and hard X-ray sources in the analyzed event, it does not explain the efficient trapping of the particles. The field line plots in Figure 12 show that the bends quickly lose their localization in the course of the upward propagation, so that any accelerated particles can easily populate large parts of these field lines. Indications for the existence of localized structures and oscillations at the apex

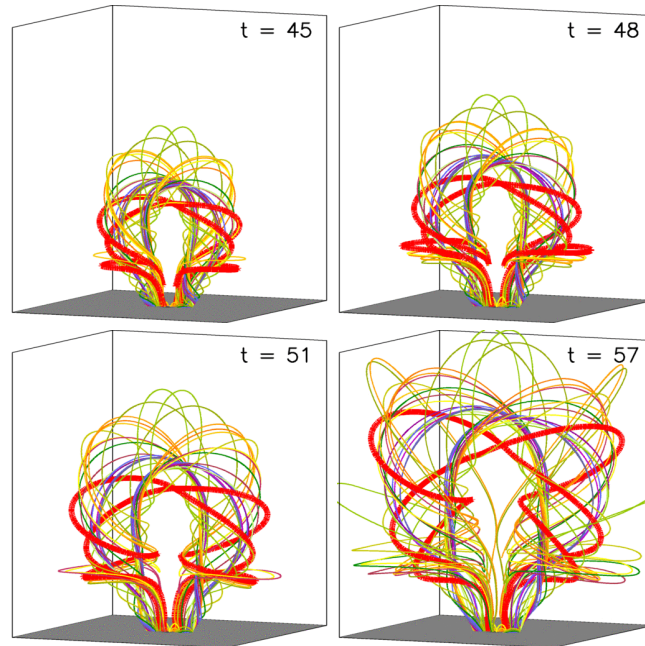


Figure 12. Formation of a relatively localized sharp bend in two symmetrical field lines at the surface of the flux rope legs by reconnection with the ambient field (thick red field lines). The bends move upward along the legs as the flux rope rises and the newly reconnected field lines relax.

of the flux rope are completely lacking. Therefore, the observations of the event do not support such a scenario.

Thus, we suggest that a scenario for the occurrence of plasmoids may be realized in some flares, which differs from the standard scenario of formation and propagation in the flare current sheet as suggested by Ohya and Shibata (1998). According to the new scenario, plasmoids can also form and propagate in a helical current sheet wrapped around strongly distorted, interacting flux ropes. In the case studied here, which requires a rather high initial twist in the flux rope, the rope interacts with itself. Plasmoids may be excited in a similar manner if a highly distorted flux rope interacts with ambient flux, which would not require such high twist.

4. Conclusions

The microwave data of the eruptive flare on 18 April 2001 in AR 9415, which originated $\approx 26^\circ$ behind the limb and was associated with a fast CME, suggest that the event involved the helical kink instability of a highly twisted flux rope. This is based on the inverse gamma shape of the microwave source as a whole and on evidence that the legs of the rising flux loop interacted (reconnected) at or near their crossing point seen projected in the plane of the sky. No other process is known that could produce both phenomena simultaneously. The evidence for

leg-leg interaction derives from the acceleration of energetic, nonthermal particles and from the formation of compact sources at or near the crossing point, which subsequently move upward along the legs of the rising flux loop.

The efficient trapping of fast particles in the compact moving microwave and hard X-ray sources suggests that these sources are plasmoids (magnetic islands in a current sheet) by nature. This interpretation is supported by their oscillations and is consistent with the motion away from their origin. Their path along the upper part of the inverse gamma source and the coalescence of multiple blobs into a final compact source at the top of the inverse gamma source are consistent with formation and propagation in the helical current sheet formed by the kink instability. Thus, the event suggests that plasmoids may form in current sheets steepened by the lateral displacement of flux tubes, in addition to the standard scenario of formation in the flare current sheet below erupting flux.

Acknowledgements The authors thank the referee for constructive comments which helped to improve the paper and T. Török for a careful reading of the manuscript. M. Karlický should like to acknowledge the support from the Nobeyama National Observatory and the kind hospitality of Prof. K. Shibasaki and his staff during his stay at Nobeyama. Furthermore, he thanks Dr. M. Shimojo for the maps presented in Figures 5 and 9. We acknowledge the HiRAS radio spectrum from the Hiraiso Solar Observatory, the use of the LASCO CME catalog, generated and maintained at the CDAW Data Center by NASA and The Catholic University of America in cooperation with the NRL, and the *SOHO* archive of EIT data. *SOHO* is a project of international cooperation between ESA and NASA. This study was supported by Grant 300030701 of Grant Agency of the Czech Academy of Sciences, by the DFG, an STFC Rolling Grant, and NASA grants NNH06AD58I and NNX08AG44G.

References

- Bárta, M., Büchner, J., Karlický, M.: 2010, *Adv. Space Res.* **45**, 10.
 Bárta, M., Vršňák, B., Karlický, M.: 2008, *Astron. Astrophys.* **477**, 649.
 Bhattacharjee, A., Huang, Y.-M., Yang, H., Rogers, B.: 2009, *Phys. Plasmas* **16**, 112102.
 Bobra, M.G., van Ballegoijen, A.A., DeLuca, E.E.: 2008, *Astrophys. J.* **672**, 1209.
 Cho, K.-S., Lee, J., Bong, S.-C., Kim, Y.-H., Joshi, B., and Park, Y.-D.: 2009, *Astrophys. J.* **703**, 1.
 Dulk, A.G.: 1985, *Ann. Rev. Astron. Astrophys.* **23**, 169.
 Edmondson, J. K. Antiochos, S. K., DeVore, C. R., Zurbuchen, T. H.: 2010, *Astrophys. J.*, in press.
 Fan, Y.: 2005, *Astrophys. J.* **630**, 543.
 Gilbert, H.R., Alexander, D., Liu, R.: 2007, *Solar Phys.* **245**, 287.
 Green, L.M., Kliem, B., Török, T., van Driel-Gesztelyi, L., Attrill, G.D.R.: 2007, *Solar Phys.* **246**, 365.
 Hudson, H.S.: 1994, in Proc. Kofu Meeting, A New Look at the Sun with Emphasis on Advanced Observations of Coronal Dynamics and Flares, ed. S. Enome and T. Hirayama (Nobeyama Radio Observatory Report 360) (Nagano, Japan: Nobeyama Radio Obs.), 1.
 Hudson, H.S., Kosugi, T., Nitta, N.V., Shimojo, M.: 2001, *Astrophys. J.* **561**, L211.
 Isenberg, P.A., Forbes, T.G.: 2007, *Astrophys. J.* **670**, 1453.
 Ji, H., Wang, H., Schmahl, E.J., Moon, Y.-J., Jiang, Y.: 2003, *Astrophys. J.* **595**, L135.
 Karlický, M.: 2004, *Astron. Astrophys.* **417**, 325.
 Karlický, M., Bárta, M.: 2007, *Astron. Astrophys.* **464**, 735.

- Karlický, M., Fárník, F., Krucker, S.: 2004, *Astron. Astrophys.* **419**, 365.
- Kliem, B., Török, T.: 2006, *Phys. Rev. Lett.* **96**, 255002.
- Kliem, B., Karlický, M., Benz, A.O.: 2000, *Astron. Astrophys.* **360**, 715.
- Kliem, B., Titov, V.S., Török, T.: 2004, *Astron. Astrophys.* **413**, L23.
- Kliem, B., Linton, M.G., Török, T., Karlický, M.: 2010, *Solar Phys.*, submitted (Paper II).
- Leboeuf, J. N., Tajima, T., Dawson, J. M.: 1982, *Phys. Fluids* **25**, 784.
- Lin, J., Forbes, T.G.: 2000, *J. Geophys. Res.* **105**, 2375.
- Lin, J., Raymond, J.C., van Ballegoijen, A.A.: 2004, *Astrophys. J.* **602**, 422.
- Loureiro, N. F., Schekochihin, A. A., Cowley, S. C.: 2007, *Phys. Plasmas* **14**, 100703.
- Magara, T., Shibata, K., Yokoyama, T.: 1997, *Astrophys. J.* **487**, 437.
- Maričić, D., Vršnak, B., Roša, D.: 2009, *Solar Phys.* **260**, 177.
- Matthaeus, W.H., Lamkin, S.L.: 1986, *Phys. Fluids* **29**, 2513.
- Min, S., Chae, J.: 2009, *Solar Phys.* **258**, 203.
- Nitta, N.: 1996, in ASP Conf. Proc. 111, Magnetic Reconnection in the Solar Atmosphere, ed. B. Bentley and J. Mariska (San Francisco: ASP), 156.
- Ohyama, M., Shibata, K.: 1997, *PASJ* **49**, 249.
- Ohyama, M., Shibata, K.: 1998, *Astrophys. J.* **499**, 934.
- Ohyama, M., Shibata, K., Yokoyama, T., Shimojo, M.: 1997, *Adv. Space Res.* **19**, 1849.
- Qiu, J., Wang, H., Cheng, C.Z., Gary, D.E.: 2004, *Astrophys. J.* **604**, 900.
- Romano, P., Contarino, L., Zuccarello, F.: 2003, *Solar Phys.* **214**, 313.
- Scholer, M., Roth, D.: 1987, *J. Geophys. Res.* **92**, 3223.
- Schrijver, C.J., Elmore, C., Kliem, B., Török, T., Title, A.M.: 2008a, *Astrophys. J.* **674**, 586.
- Schumacher, J., Kliem, B.: 1996, *Phys. Plasmas* **3**, 4703.
- Schumacher, J., Kliem, B.: 1997, *Phys. Plasmas* **4**, 3533.
- Shibata, K., Tanuma, S.: 2001, *Earth. Planets Space* **53**, 473.
- Shibata, K., Masuda, S., Shimojo, M., Hara, H., Yokoyama, T., Tsuneta, S., Kosugi, T., Ogawara, Y.: 1995, *Astrophys. J.* **451**, L83.
- Švestka, Z., Fárník, F., Hudson, H.S., Uchida, Y., Hick, P., Lemen J.R.: 1995, *Solar Phys.* **161**, 331.
- Temmer, M., Veronig, A.M., Vršnak, B., Rybák, J., Gömöry, P., Stoiser, S., Maričić, D.: 2008, *Astrophys. J.* **673**, L95.
- Török, T., Kliem, B.: 2005, *Astrophys. J.* **630**, L97.
- Török, T., Kliem, B.: 2007, *Astron. Nachr.* **328**, 743.
- Tsuneta, S., Masuda, S., Kosugi, T., Sato J.: 1997, *Astrophys. J.* **478**, 787.
- Vršnak, B., Ruždjak, V., Rimpolt, B.: 1991, *Solar Phys.* **136**, 151.
- Vršnak, B., Ruždjak, V., Rimpolt, B., Roša, D., Zlobec, P.: 1993, *Solar Phys.* **146**, 147.
- Williams, D.R., Harra, L.K., Brooks, D.H., Imada, S., Hansteen, V.H.: 2009, *Pub. Astron. Soc. Japan*, **61**, 493.
- Zhang, J., Dere, K.P.: 2006, *Astrophys. J.* **649**, 1100.